JGR Planets

RESEARCH ARTICLE
10.1029/2025JE008948

Secular Change of Preservation of Lunar Sinuous Rilles: Constraints From Lava Flow Numerical Modeling

Xuanyu Deng[1], Wei Tian[1], Yuqi Qian[2], Craig Magee[3], Zhongbo Gao[1], Zihan Wei[4], Jiaqi Fang[5], Lisong Qiu[1], Zilong Wang[1], Lei Wang[1], Wei-(RZ) Wang[6], and Yonggang Liu[7]

[1]School of Earth and Space Sciences, Peking University, Beijing, China, [2]Department of Earth Sciences and Laboratory for Space Research, The University of Hong Kong, Hong Kong, China, [3]School of Earth and Environment, University of Leeds, Leeds, UK, [4]Department of Geophysics, Stanford University, Stanford, CA, USA, [5]Seismological Laboratory, California Institute of Technology, Pasadena, CA, USA, [6]Institute of Geomechanics, Chinese Academy of Geological Sciences, Beijing, China, [7]School of Physics, Peking University, Beijing, China

Key Points:

- The mare volcanism changes from an early intense peak to a late mild surge, with the latter favoring the preservation of sinuous rilles
- We establish a Bingham flow model of basaltic lava based on Chang'e-5 samples and constrain eruptive limits for preserving sinuous rilles
- The pre-existing sinuous rilles can be greatly modified by lava flows, diminishing their depth and continuity

Supporting Information:

Supporting Information may be found in the online version of this article.

Correspondence to:

W. Tian,
davidtian@pku.edu.cn

Citation:

Deng, X., Tian, W., Qian, Y., Magee, C., Gao, Z., Wei, Z., et al. (2026). Secular change of preservation of lunar sinuous rilles: Constraints from lava flow numerical modeling. *Journal of Geophysical Research: Planets*, *131*, e2025JE008948. https://doi.org/10.1029/2025JE008948

Received 24 JAN 2025
Accepted 15 MAR 2026

Author Contributions:

Conceptualization: Xuanyu Deng, Wei Tian, Yuqi Qian
Data curation: Xuanyu Deng, Zilong Wang, Lei Wang
Formal analysis: Zilong Wang, Wei-(RZ) Wang
Funding acquisition: Wei Tian
Investigation: Xuanyu Deng, Wei Tian, Yuqi Qian, Zilong Wang, Yonggang Liu
Methodology: Xuanyu Deng, Wei Tian, Zhongbo Gao, Zihan Wei, Jiaqi Fang, Lisong Qiu, Lei Wang, Yonggang Liu
Project administration: Wei Tian
Software: Xuanyu Deng, Zhongbo Gao, Jiaqi Fang, Lisong Qiu, Lei Wang
Supervision: Wei Tian
Validation: Xuanyu Deng, Zhongbo Gao, Zihan Wei, Jiaqi Fang, Lisong Qiu, Lei Wang
Visualization: Xuanyu Deng, Yuqi Qian, Craig Magee, Jiaqi Fang
Writing – original draft: Xuanyu Deng

Abstract Lunar mare basalts, produced by the partial melting of the lunar mantle, provide key insights into volcanic activity and thermal evolution of the Moon. China's lunar exploration mission, Chang'e-5 (CE-5), sampled mare basalts in the Northern Oceanus Procellarum, close to a sinuous rille, Rima Sharp. Sinuous rilles are meandering channel-like depressions formed by basaltic lava flows; however, their origin and evolution remain debatable, even though nearly 200 examples have been identified. Here, we use Cellular Automata to explore how lunar basaltic lava flows dictate the preservation potential of pre-existing sinuous rilles. Specifically, we model lavas as Bingham fluids, constrained by physical properties of the returned CE-5 sample, that flow on a sloped plane and interact with rilles of different sinuosities (i.e., degrees of meandering). Our results show that most rilles are preserved when eruptions last 10^5 s (~1 day) at effusion rates of 1.2×10^4–8×10^4 m^3/s, that is, mare regions hosting sinuous rilles likely did not experience intense volcanic activities since rille formation. We also recognize an increase in the area density of sinuous rilles—total rille lengths per unit area of mare basalts—through time that is consistent with our modeling. Overall, our findings suggest that early stage volcanism on the Moon (3.8–3.4 Ga) was more intense and had lower preservation potential of rilles than a milder late stage (2.0–1.2 Ga). These findings constrain the preservation conditions of rilles, offering new insights into their evolution and contributing to a broader understanding of lunar volcanic and thermal history.

Plain Language Summary Lunar sinuous rilles are long, winding channels on the surface of the Moon that resemble rivers on Earth. Instead of being shaped by water, sinuous rilles are carved by lava flows. China's lunar exploration mission, Chang'e 5, landed in a region of lunar lavas where the longest sinuous rille, Rima Sharp, passes through. The returned lunar soil sample gives us an opportunity to study the evolution of sinuous rilles and lunar volcanism. Just as terrestrial river courses may be submerged by floods, sinuous rilles may also be changed or destroyed by later lava flows. Here we simulate the lava flows that have physical properties informed by the CE-5 sample to explore whether sinuous rilles may be buried or preserved during later eruptions. The preservation potential of sinuous rilles can further reflect the intensity of lunar volcanism. With milder eruptive events, which are common in the late stage of lunar volcanism in the past 2 billion years, sinuous rilles are more likely to remain well-preserved.

1. Introduction

Unraveling the volcanic history of the Moon is crucial to understanding its thermal evolution (Spohn et al., 2001; Shearer et al., 2006; Wilson & Head, 2017). The mare basalts, which cover ~17% of the lunar surface, show a substantial range in crater size-frequency model ages and thus provide an archive of lunar volcanism (Figure 1a) (Head & Wilson, 1992; Hiesinger et al., 2011; Qian et al., 2023). Mare volcanism since the Imbrian (from 3.8 Ga onward) can be divided into four broad stages (Head et al., 2023), with an early peak (Stage I) of basalt emplacement during the Imbrian, and a late surge (Stage IV) during the Eratosthenian (Figure 1b) (Du et al., 2022; Hiesinger et al., 2011; Tian et al., 2023). These long-term stages describe the global evolution of mare volcanism over billions of years. To interpret the dynamics of individual eruptions within these broader stages, a four-phase eruptive model for lunar basaltic volcanism was proposed by Wilson and Head (2018). In this conceptual framework, Phase 1 represents the onset of eruptions, characterized by a transient release of gas;

Writing – review & editing:
Xuanyu Deng, Wei Tian, Yuqi Qian, Craig Magee, Zihan Wei, Jiaqi Fang, Zilong Wang, Wei-(RZ) Wang, Yonggang Liu

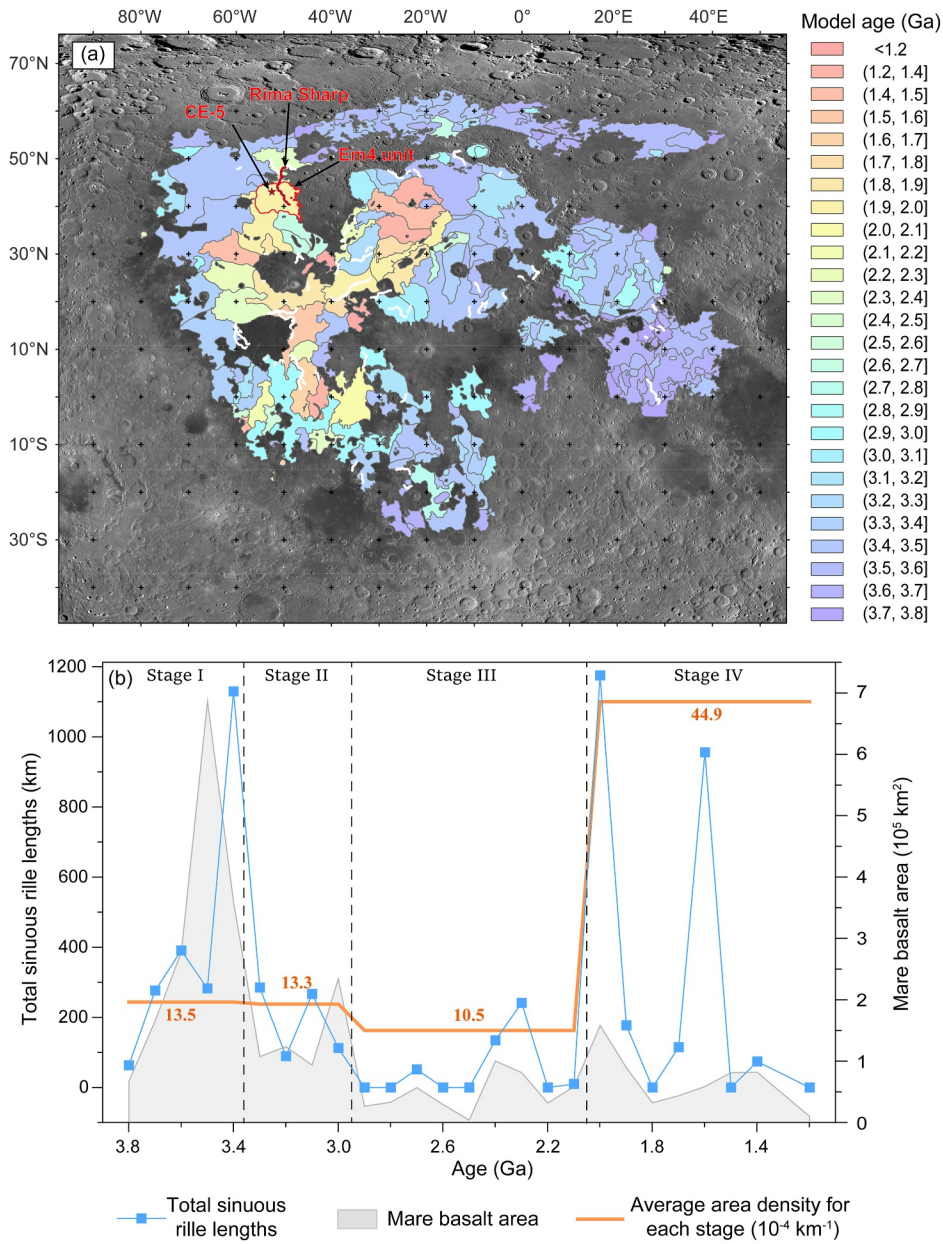

Figure 1. A statistical analysis of the mare basalt units and all the mapped sinuous rilles (72 in total) situated on these units: (a) Model ages of mare basalts and locations of mapped sinuous rilles (white curved lines). The red line is Rima Sharp and the red star is the sampling point of CE-5 mission. The mare unit outlined by the red boundary corresponds to the Em4 basalt unit. Data from Hiesinger et al. (2011), Hurwitz et al. (2013), and Qian et al. (2023). For the sinuous rilles crossing several mare units, we choose the age of the latest mare unit that it crosses through as its age. (b) The temporal change of the total sinuous rilles length (blue square) and mare basalt area (gray) at 0.1 Ga intervals, and the average area density (orange line) of four distinct stages of mare volcanism. We assume that the spatial distribution of rilles is uniform even after partial burial. Stage I: Peak stage (3.8–3.4 Ga); Stage II: Steep decline stage (3.3–3.0 Ga); Stage III: Trough stage (2.9–2.1 Ga); and Stage IV: Late surge stage (2.0–1.2 Ga). See Data Set S1 in Supporting Information S2 for original data.

Phase 2 is the high-flux Hawaiian phase under an effusion rate of 10^5–10^6 m^3/s; Phase 3 exhibits a decrease in flux (10^4–10^5 m^3/s); and Phase 4 represents the wanning of eruptions. Within mare basalts, sinuous rilles are unique volcanic landforms that comprise elongated and meandering channel-like depressions associated with thermally or mechanically induced erosional and constructional structures (Hurwitz et al., 2012; Roberts & Gregg, 2019; Williams et al., 2000). Analyses of these sinuous rilles and potential terrestrial analogs suggest that they represent (partly) collapsed subsurface lava tubes indicative of high effusion rate (10^5–10^6 m^3/s) volcanism

akin to Hawaiian style eruptions (Greeley, 1971; Wilson & Head, 2018). Constraining when sinuous rilles developed, and assessing their preservation potential, can therefore help determine eruption fluxes and magma supply through lunar history.

To characterize when sinuous rille formation and preservation were prevalent, and their relationship with mare volcanism, we separate the lunar volcanic history into 0.1 Ga intervals and for each calculate the total area of mare basalts and total lengths of sinuous rilles. By dividing the cumulative sinuous rille length by the corresponding mare basalt area for each stage, we estimated the **average area density** of sinuous rilles (Figure 1b). Although most sinuous rilles and mare basalts are observed to emplace during Stage I, the area density of this stage is less than that of Stage IV according to our statistics. This contrast suggests that it is this area density, not the quantity or lengths, of sinuous rilles, that best captures their preservation potential.

We explore how the preservation potential of sinuous rilles may impact our area density calculations by incorporating lava properties measured from China's lunar exploration mission Chang'e-5 (CE-5) sample. Rima Sharp extends primarily across the Em4 basalt unit, a series of lava flows emplaced ∼2.0 Ga, in the Northern Oceanus Procellarum where CE-5 collected samples (Figure 1a) (Qian, Xiao, Head, van der Bogert, et al., 2021). Although we did not model the evolution of Rima Sharp itself, its proximity to the sampling site allows the CE-5 basalts to serve as a representative reference for the lava involved in rille formation and preservation. Specifically, we construct a Cellular Automata model that simulates the flow of a Bingham fluid (lava), with physical properties obtained from the returned lunar sample (CE5C0800YJYX005GP, hereinafter referred to as 005GP), to test how eruptive parameters (effusion rate and eruptive duration) control whether pre-existing sinuous rilles either become infilled or remain well-preserved.

2. Methods

We aim to model how lunar lava flows interact with pre-existing sinuous rilles to test what eruptive conditions are required to preserve or bury the rilles. Lava flows are complex and evolving systems in which temperature, rheology, and kinematics vary both spatially and temporally (Barca et al., 1993; Crisci et al., 1986). Such a system can be simulated by Cellular Automata, a science modeling technique that has been successfully applied to the study of terrestrial volcanoes (e.g., Cappello et al., 2022; Miyamoto & Sasaki, 1997; Vicari et al., 2007). This technique is also suitable for lunar applications, as mare basalts share similar effusive behavior and low viscosity with terrestrial basaltic flows, such as those observed in Hawaii. In the sections that follow, we outline the structure and workflow of Cellular Automata, formulas for material and heat flux calculations, and physical and eruptive parameters used in the simulations, including adaptations made for lunar volcanism.

2.1. Cellular Automata Modeling Setup

The Cellular Automata in our model contains a 2D computational plane with a slope of 0.1° (Figure 2), which is the measured average slope of the Em4 unit (Qian, Xiao, Head, van der Bogert, et al., 2021). The computational domain is discretized with 600×600 square cells of 500 m length. We define five volcanic vents. Four of them are located 2.5 km from four pre-existing sinuous rilles, each with a uniform depth of 60 m and a width of 3 km. The remaining vent, which is not associated with a rille, serves as a control (Figure 2). Sinuosity of the pre-existing rilles is variable and calculated as the ratio of the rille line length to its tip-to-tip straight-line distance (Leroux, 1992). As the sinuosity of observed sinuous rilles ranges from 1.03 to 2.09 with an average value of 1.22 (Hurwitz et al., 2013), we set our four rilles to have sinuosities of 1.0, 1.1, 1.3 and 1.6, corresponding to three categories: nearly straight (R1), slightly sinuous (R2 and R3), and highly sinuous (R5) rilles (Figure 2).

The cell states, representing lava *thickness* (H) and *temperature* (T), can change through time according to evolution functions, which here are the material and heat fluxes; that is, lava can move from one cell to a neighboring cell if the magma supply is sufficient and it has not cooled enough to solidify. The evolution function of the material flux relates to the Navier-Stokes (N-S) equation, which strongly depends on the geometric shape of cells and the flow direction relative to the symmetrical axis of cells (Vicari et al., 2007). To eliminate this artificial anisotropy, we have employed a Monte-Carlo approach to define which of the eight neighbors of any cell material can flow to (see Text S1 and Figure S1 in Supporting Information S1).

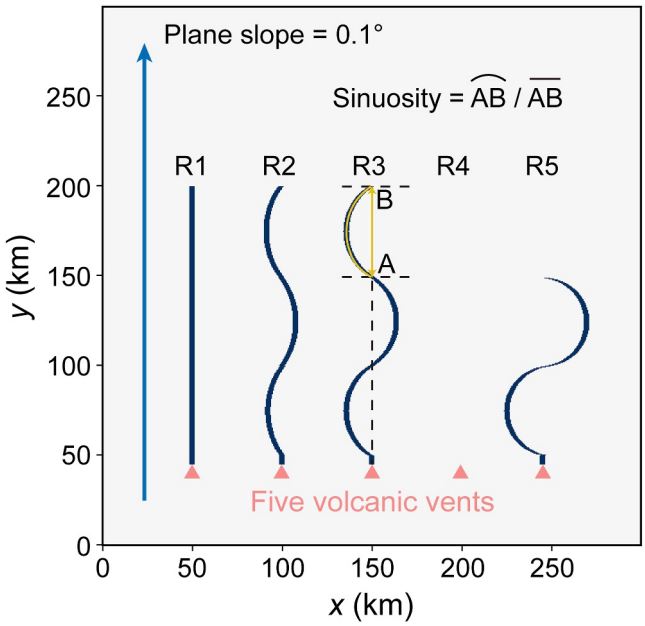

Figure 2. Initial settings and map-view perspective of model construction. The plane slope was 0.1°. Four pre-existing sinuous rilles (R1, R2, R3, and R5) are modeled, each with constant depths of 60 m relative to the local plane height outside the rilles but distinctive sinuosities. R4 serves as a control case without rilles. The widths of sinuous rilles we defined remain consistent in the direction perpendicular to the slope's descent. Pink triangles denote five volcanic vents, each comprising a grid of four adjacent computational cells.

2.2. Defining a Bingham Fluid Model

Lava is generally considered to flow like a Bingham fluid (Dragoni et al., 1986; Griffiths, 2000; Robson, 1967), that is, the fluid flows only when the shear stress exceeds its yield strength σ_y. For Bingham-like lavas, the upper part of the fluid, termed the *plug* (Figure 3a), does not undergo the shear deformation because the applied stress is less than σ_y. The thickness of the *plug* represents the critical thickness (H_c) of lava, such that lava can only flow if its thickness (H) exceeds H_c (Dragoni et al., 1986). By considering how lavas flow on inclined planes due to gravity and pressure gradients induced by thickness variations, we can estimate the volumetric lava flow rate (q) in our model as (see Text S2 in Supporting Information S1 for a detailed derivation):

$$q = \frac{\sigma_y H_c^2 \Delta x}{3\eta}\left[\left(\frac{H}{H_c}\right)^3 - \frac{3}{2}\left(\frac{H}{H_c}\right)^2 + \frac{1}{2}\right], H \geq H_c \tag{1}$$

where Δx is the cell width and η is the dynamic viscosity of lava (Dragoni et al., 1986; Miyamoto & Sasaki, 1997). The critical thickness can be expressed as (Cappello et al., 2022; Miyamoto & Sasaki, 1997):

$$H_c = \frac{\sigma_y}{\rho g\left(\sin\alpha - \frac{\partial H}{\partial x}\cos\alpha\right)} = \frac{\sigma_y\sqrt{\Delta x^2 + \Delta z^2}}{\rho g(\Delta z + \Delta h)} \tag{2}$$

where ρ is the density of lava (temperature-dependent, Table S1 in Supporting Information S1), α is the plane slope, Δz and Δh are the differences in basal elevation and thickness between two cells (Figure 3b). The thickness of cells at time $t + \Delta t$ ($H_{t+\Delta t}$) follows:

$$H_{t+\Delta t} = H_t + \sum_i \frac{q_i \Delta t}{\Delta x^2} \tag{3}$$

where H_t is the thickness of cells at time t, q_i is the volumetric flow rate between the central cell (for which the state is being updated, Figure S1 in Supporting Information S1) and its ith neighbor, and Δt is the timestep. The change in lava thickness within the timestep Δt should be less than H_t to ensure the validity of a steady state solution of the N-S equation. From this condition, a constraint on the timestep follows (Bilotta et al., 2012; Vicari et al., 2007):

$$\Delta t < \min_{\text{all cells}}\left(\frac{c\Delta x^2 H_t}{q}\right) \tag{4}$$

where c is a parameter (called Courant Number) used to balance accuracy and efficiency within the limits imposed by numerical stability (Courant et al., 1928; Liu, 2020). The value we chose is $c = 0.08$. Since the condition in Equation 4 should be satisfied for each cell, the minimum timestep over all cells is used.

To define the temperature of lava in each cell (T), we consider that, due to the lack of a lunar atmosphere, heat transfer between lava and the environment occurs only through radiative heat loss ($\Delta Q_{t,r}$) (Griffiths & Fink, 1992):

$$\Delta Q_{t,r} = \epsilon S \sigma_{SB}\left(T^4 - T_a^4\right)\Delta t \tag{5}$$

where ϵ is the emissivity of lava, σ_{SB} is the Stefan-Boltzmann constant, T_a is the radiative background temperature. It is set to 250 K and corresponds to the average temperature of the lunar surface, to which heat is lost (Williams et al., 2017). S is the radiative heat loss area exposed to the environment within each cell. Unlike the projected horizontal area ($S_0 = \Delta x^2$) used in Vicari et al. (2007), we correct the radiative area to account for

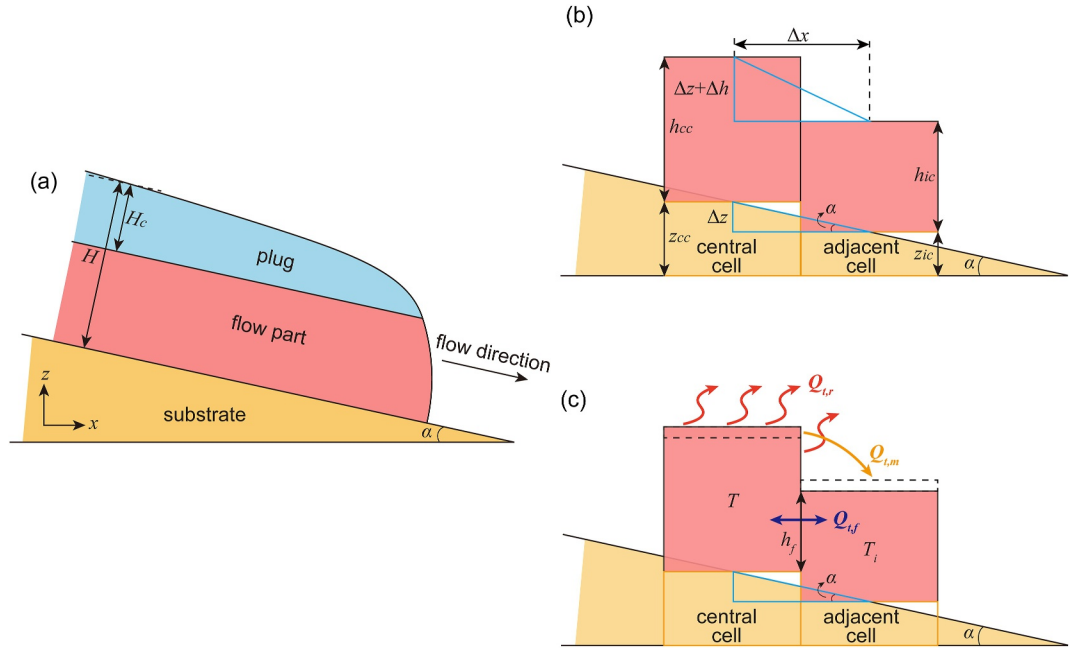

Figure 3. (a) Schematic cross-section for a Bingham flow. The flow is divided into two parts, with a stationary *plug* above and a flowing part below. Figure modified from Miyamoto and Sasaki (1997). (b) Local reference system for calculating H_c. h_{cc} and h_{ic} denote lava thicknesses of the central cell and the adjacent cell, respectively, whereas z_{cc} and z_{ic} denote their corresponding cell basal elevations. Thus, the differences in basal elevation and thickness between two cells in Equation 2 are defined as $\Delta z = z_{cc} - z_{ic}$, and $\Delta h = h_{cc} - h_{ic}$, respectively. (c) Heat fluxes in the model. Radiative heat loss occurs from the exposed lava surface, which for each cell includes its top horizontal surface and portions of the lateral surface exposed by offset of adjacent cells. Conductive heat transfer occurs across the intercell contact surface. h_f is the contact height between cells, which is calculated as $h_{ic} - (z_{cc} - z_{ic})$. Advective heat transfer corresponds to thermal energy transported by lava mass flux between cells. The dashed line indicates changes in bulk lava thickness related to the movement of lava within the timestep Δt and does not represent surface flow.

variations in lava thickness, especially near flow margins, so that S exceeds S_0 (Text S3 in Supporting Information S1).

The total heat transfer (ΔQ) in each cell also includes advective heat transfer ($\Delta Q_{t,m}$) carried by lava flowing in or out of the cell, and conductive heat transfer ($\Delta Q_{t,f}$) between adjacent cells driven by temperature gradients (Figure 3c). Heat conduction to the subsurface can be neglected for the bulk flow dynamics (Harris & Rowland, 2015; Ortega-Moya et al., 2024) because of the low thermal conductivity of lunar regolith (Xiao et al., 2022; Yu & Fa, 2016). We verified this assumption through a comparative calculation (Text S4 and Figure S2 in Supporting Information S1) (Turcotte & Schubert, 2014). For simplicity, we also neglect vertical temperature variations and the temperature in a cell is considered uniform (Vicari et al., 2007). Thus, we have:

$$\Delta Q = Q_{t+\Delta t} - Q_t = \Delta Q_{t,m} + \Delta Q_{t,f} - \Delta Q_{t,r} \tag{6}$$

with:

$$\Delta Q_{t,m} = \left(\sum_{q_i > 0} q_i T_i + \sum_{q_i < 0} q_i T \right) \rho c_p \Delta t \tag{7}$$

and:

$$\Delta Q_{t,f} = \sum_i \kappa h_f (T_i - T) \Delta t \tag{8}$$

where T and T_i are the temperatures of the central cell and its ith neighbors, c_p is the specific heat capacity of lava per unit mass, κ is the thermal conductivity of lava, and h_f is the contact height of lava between two cells (Figure 3c). We assume that the internal energy of lava is given by the product of specific heat capacity, mass, and temperature. Therefore, the second state of cells can be updated as

$$T_{t+\Delta t} = \frac{Q_{t+\Delta t}}{\rho c_p H_{t+\Delta t} S_0} \tag{9}$$

The two evolution functions defined above, Equations 3 and 9, update cell states in our Cellular Automata model. At the model onset ($t = 0$), the lava thickness of each cell is set to zero and the temperature is set to the radiative background temperature ($T_a = 250$ K). We then define several cells as volcanic vents, which start to discharge lava at an effusion rate of u_t. When the thickness (H) of lava at the vent cell exceeds its critical thickness (H_c), lava can spread to adjacent cells. Within each timestep, state updates are applied to all lava-containing cells, together with randomly selected neighboring cells adjacent to the flow front (Text S1 and Figure S1 in Supporting Information S1), until the model ends (t = SumTime). The overall workflow is shown in Figure 4 (see Text S5 and Table S1 in Supporting Information S1 for details of model execution).

2.3. Parameter Settings

The sampling site of CE-5 mission is located in the Em4 unit of the Northern Oceanus Procellarum, ~15 km from Rima Sharp (Qian, Xiao, Head, & Wilson, 2021). The returned lunar soil samples of CE-5 are considered to represent the volcanic materials of the Em4 unit on the basis of spectral elemental data from the orbit (Qian, Xiao, Head, van der Bogert, et al., 2021). The CE-5 basalt clast studied in this work is from the soil sample 005GP, weighing 16.6 mg. The major element compositions of 005GP were determined by electron microprobe analysis, and the analytical procedures are described in Text S6 in Supporting Information S1. Assuming that the sinuous rille lavas are the same as the mare basalts, we use the major element compositions of 005GP to determine the rheological parameters of our modeled basaltic lava flow (Table 1).

A key parameter for our modeling is lava viscosity, which we can parameterize from the temperature, major element compositions and water contents of magma (Giordano et al., 2008):

$$\log \eta = A + \frac{B}{T - C} \tag{10}$$

where adjustable parameters A, B, and C are −4.55, 5051.6, and 676.3 respectively, calculated by major element compositions of 005GP. The water contents of returned CE-5 samples range from several tens to over one hundred ppm, which is sufficiently low to be neglected in the viscosity calculations (Lin et al., 2024; Liu et al., 2022). For the yield strength, we consider (Dragoni, 1989):

$$\sigma_y = \sigma_{y0}\left[e^{b(T_l - T)} - 1\right] \tag{11}$$

where T_l is the liquidus temperature, which is 1,407.15 K as calculated by MELTS (Ghiorso et al., 2002), and σ_{y0} and b are the constants with the values of 0.01 Pa and 0.08 K^{-1}, respectively (Dragoni, 1989). Petrological evidence and crystallization history studies indicate that the CE-5 basaltic magma underwent a rapid ascent and eruption from a shallow magma chamber in the lunar crust (e.g., Luo et al., 2023; Wang et al., 2023), supporting our use of a liquidus-near eruption temperature (1,400 K) in the model. With decreasing temperature, lava viscosity and yield strength increased (Figure 5).

Another parameter characterizing the lava flow process is the *effusion rate* u_t, which is the instantaneous volume flux at the source vent (Harris et al., 2007). In terrestrial settings, we commonly observe eruptions have a high initial effusion rate that approximately decreases exponentially (e.g., Gudmundsson, 2020; Harris et al., 2000; Machado, 1974; Thordarson & Larsen, 2007):

$$u_t = u_0 e^{-kt} \tag{12}$$

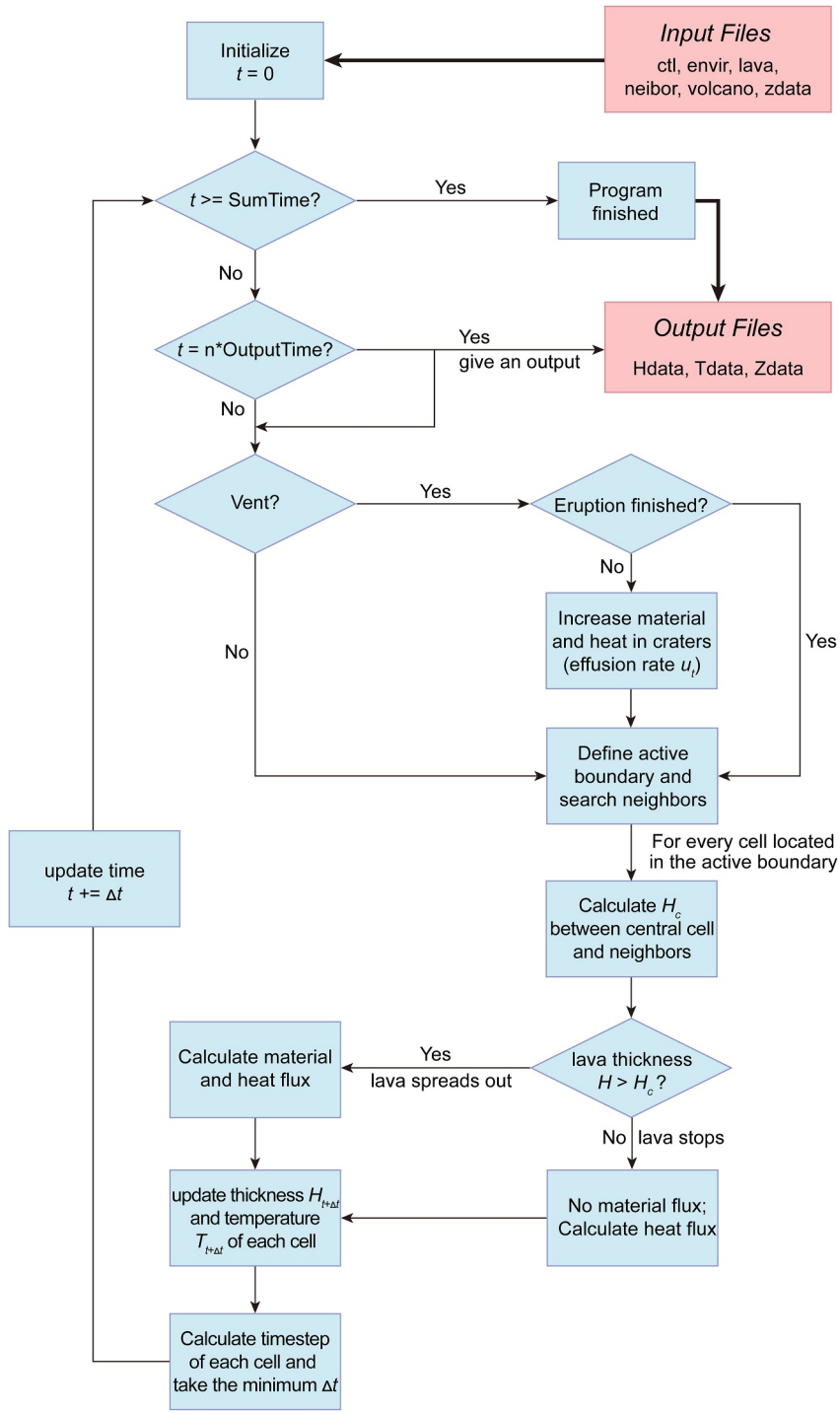

Figure 4. The workflow of our model.

Table 1
Major Element Compositions of the CE-5 Sample (005GP)

	SiO_2	TiO_2	Al_2O_3	Cr_2O_3	FeO	MnO	MgO	CaO	Na_2O	K_2O	P_2O_5
Contents (wt %)	42.71	5.91	10.50	0.14	22.72	0.28	4.80	10.85	0.57	0.25	0.28
s.d. (%)	0.09	0.02	0.04	0	0.14	0.01	0.06	0.05	0.02	0.02	0

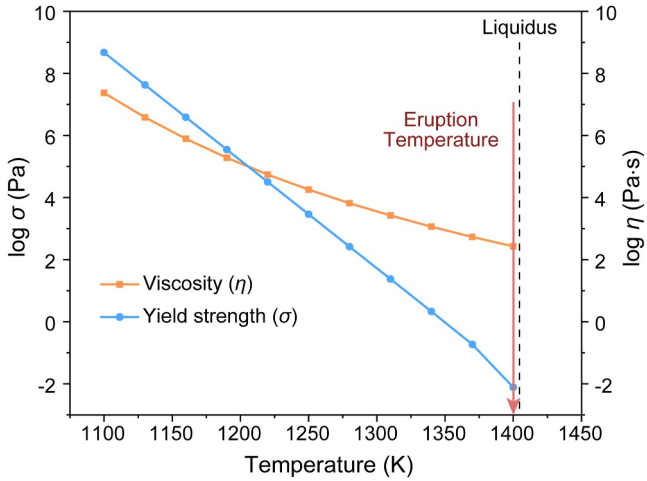

Figure 5. The viscosity (orange square) and yield strength (blue circle) of CE-5 magma as a function of temperature. The eruption temperature was set to 1,400 K.

where u_0 is the initial rate and k is a constant that depends on the excess pressure, compressibility, magma reservoir volume, and feeder-dike geometry (Gudmundsson, 2020). For modeling convenience, we assume that lunar eruptions follow an exponentially decreasing effusion rate, analogous to terrestrial eruptions. In our model, a single lunar eruptive phase thus consists of two episodes—a constant-effusion-rate episode and a decreasing-effusion-rate episode where the effusion rate is exponentially decreasing (Figure 6). The transition from Phase 2 to Phase 3 involves an exponential decrease in effusion rate, which may occur either directly or after a temporary stop in activity (Figure 6) (Gudmundsson, 2020). Additional input parameters used in the model are reported in Table 2.

3. Results

Following the sequential eruption phase model proposed by Wilson and Head (2018), our modeling specifically examines the eruptive conditions representative of Phases 2 and 3. We varied the effusion rate (4×10^3–4×10^6 m^3/s) and duration (5×10^4, 10^5, and 2×10^5 s) of the constant-effusion-rate episode in both Phase 2 and Phase 3 to investigate their effects on the preservation of sinuous rilles (Figure 6). To quantify these effects, we define the ***infilled SR length*** as the portion of the rille over which new lava has flowed but where its upper surface remains beneath the rille top, that is, rilles remain preserved. We likewise define the ***overflow stage*** as the condition in which the new lava completely fills the rille and spills out onto the surrounding surface, that is, rilles become buried. The results reveal clear differences between low- and high-flux eruptions, showing when lava tends to stay within the rilles and when it spreads across the surrounding surface. Finally, we present a sensitivity analysis of two model input parameters—plane slope and computational cell width—to evaluate the robustness of our simulation outcomes.

3.1. Preservation of Sinuous Rilles During Low-Flux Eruptions (Phase 3)

We first conducted 14 groups of simulations (Groups 1–14 in Table 3) where effusion rates of the constant-effusion-rate episode range from 4×10^3 to 2.4×10^5 m^3/s over a period of 10^5 s, followed by a decreasing-effusion-rate episode lasting 6×10^4 s. All simulation groups were terminated at 2×10^5 s (SumTime), by which time lava motion had ceased. Snapshots of all groups, recorded every 10^4 s up to SumTime, are presented in Data Set S2 in Supporting Information S3. At an effusion rate of 4×10^3 m^3/s (Group 1), lava remains localized around the vents (Figure 7a). When the effusion rate increases to 2×10^4 m^3/s (Group 4), lava begins to flow along rille R1, R2, and R3 (blue dashed rectangles in Figure 7b), but overflows rille R5 (red dashed rectangles in Figure 7b). At an effusion rate of 4×10^4 m^3/s (Group 6), lava flows along rille R1 and R2 (blue dashed rectangles in Figure 7c), but overflows rille R3 and R5 (red dashed rectangles in Figure 7c). When the effusion rate reaches 2×10^5 m^3/s (Group 13), lava floods all rilles (red dashed rectangles in Figure 7d). The maximum infilled SR length (Table 3) first increases with the effusion rate when the rate is below 8×10^4 m^3/s, and then decreases and fluctuates at higher effusion rates (Figure 7e).

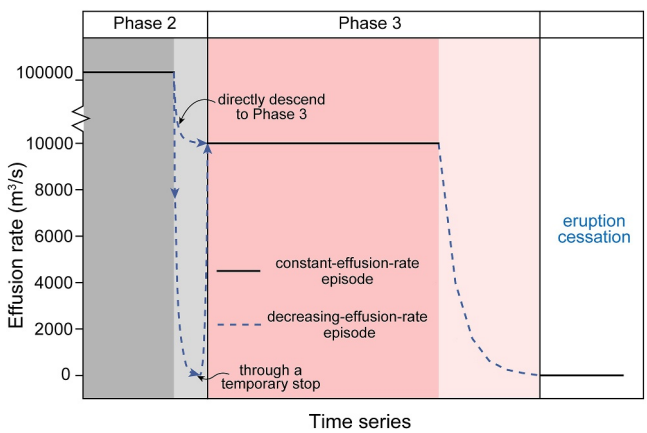

Figure 6. Eruptive phases of lunar volcanoes. The dashed lines with arrows indicate two possible ways after Phase 2 (Gudmundsson, 2020). Each eruptive phase consists of a constant-effusion-rate episode (solid black line) and a decreasing-effusion-rate episode (dashed blue line).

We also examined how different durations of the constant-effusion-rate episode affected the preservation of sinuous rilles (Groups 15–23 in Table 3). Three sets of eruptive durations were tested—5×10^4, 10^5, and 2×10^5 s—each followed by a decreasing-effusion-rate episode lasting 6×10^4 s, giving a SumTime of 1.5×10^5, 2×10^5, and 3×10^5 s, respectively. These are hereafter referred to as Sets A, B, and C. For each set, three simulation groups were performed using different effusion rates of 2×10^4, 4×10^4, and 8×10^4 m^3/s in the constant-effusion-rate episode. Table 3 lists the maximum infilled SR lengths of each group. All time-step snapshots of

Table 2
Parameters Used in Our Model

Parameter	Symbol	Value	Unit	Reference
Density of lava	ρ	Temperature-dependent (dynamically updated in the simulation, see Table S1 in Supporting Information S1)	kg m^{-3}	Bottinga and Weill (1970)
Liquidus of lava	T_l	1,407.15	K	\
Cell width	Δx	500	m	\
Emissivity of lava	ϵ	0.9	\	Griffiths and Fink (1992)
Stefan-Boltzmann constant	σ_{SB}	5.67×10^{-8}	W m^{-2} K^{-4}	\
Radiative background temperature	T_a	250	K	Williams et al. (2017)
Specific heat capacity of lava	c_p	1,200	J kg^{-1} K^{-1}	Neri (1998)
Thermal conductivity of lava	κ	2.0	W m^{-1} K^{-1}	Neri (1998)
Density of lunar regolith	ρ_g	1,500	kg m^{-3}	Carrier et al. (1991)
Specific heat capacity of lunar regolith	$c_{p,g}$	670	J kg^{-1} K^{-1}	Keihm (1984)
Thermal conductivity of lunar regolith	κ_g	10^{-4}–0.03	W m^{-1} K^{-1}	Yu and Fa (2016)
Lunar gravitational acceleration	g	1.62	m s^{-2}	\

Groups 15–23, recorded every 10^4 s until the SumTime, are presented in Data Set S2 in Supporting Information S3. Figure 8 illustrates the temporal evolution of the infilled SR length of rille R2. In Set A (5×10^4 s of eruptive duration, Figure 8a), the infilled SR length increases with time in all three groups and stabilizes at 25, 42, and 56 km for effusion rates of 2×10^4, 4×10^4, and 8×10^4 m^3/s, respectively (Groups 15–17). In Set B (10^5 s, Figure 8b), Groups 18 and 19 (with effusion rates of 2×10^4 and 4×10^4 m^3/s) exhibit similar trends, reaching a final length of 35 and 52 km, respectively. However, Group 20 (8×10^4 m^3/s) attains a maximum length of 58 km and then decreases to 44 km in the end. In Set C (2×10^5 s, Figure 8c), only Group 21 (2×10^4 m^3/s) exhibits a continuous increase, stabilizing at 43 km, whereas Groups 22 and 23 (4×10^4 and 8×10^4 m^3/s) both show an initial growth followed by a decline of the infilled SR length, ending at 30 and 43 km, respectively.

3.2. Preservation of Sinuous Rilles During High-Flux Eruptions (Phase 2)

Section 3.1 demonstrates how variations in effusion rate influence the preservation of sinuous rilles under a low effusion rate (10^3–10^5 m^3/s). We conducted another two groups of simulations (Groups 24–25, Table 3) to investigate rille preservation during high-flux eruptions (with effusion rate of 10^5–10^6 m^3/s in the constant-effusion-rate episode of Phase 2). At an effusion rate of 4×10^5 m^3/s (Figure 9a), lava periodically overflows the rille R1 and R2 along part of their length (same as Figure 7d). As for R3 and R5, lava behaves like a sheet flow and buries most of the near-vent rille up to 60 km, showing a flow pattern similar to that in the control case R4. When the rate increases to 4×10^6 m^3/s (Figure 9b), lava consistently reshapes the initial plane like a sheet flow in all cases, yet the pre-existing rilles (R1, R2, R3, and R5) are not completely buried but preserved in the face of intense lava flows.

To further examine how sheet-like lava flows modify rille morphology, we selected three cross sections at the proximal, medial and distal parts of R2 in Figure 9b, as shown in Figure 10a. We find that the preserved rille becomes shallower with increasing distance from the vents, eventually disappearing at the distal end (*CC'* section in Figure 10a). To illustrate this downstream shallowing trend more clearly, we extract a longitudinal profile of R1 in Figure 10b, with orange line showing the average thickness of lava spilled over the surrounding terrain of the rille and green line depicting the average lava thickness within the rille. Therefore, the difference between these two lines denotes the modified rille depth. We find that the original 150-km-long rille has been separated into three segments, which modified rille depths progressively decrease downstream, consistent with periodic overflow of lava.

Table 3
Summary of Modeling Parameters and the Maximum Infilled SR Length of Simulation Groups

Group number		Effusion rate (m^3/s)	Eruptive duration (s)	Maximum infilled SR length (km)
1		4×10^3	10^5	5.00
2		1.2×10^4	10^5	8.50
3		1.6×10^4	10^5	22.68
4		2×10^4	10^5	31.75
5		3×10^4	10^5	36.76
6		4×10^4	10^5	44.96
7		5×10^4	10^5	53.73
8		6×10^4	10^5	58.50
9		7×10^4	10^5	68.84
10		8×10^4	10^5	69.92
11		1.2×10^5	10^5	38.37
12		1.6×10^5	10^5	33.15
13		2×10^5	10^5	41.00
14		2.4×10^5	10^5	29.33
Set A	15	2×10^4	5×10^4	24.72
	16	4×10^4	5×10^4	42.36
	17	8×10^4	5×10^4	56.29
Set B	18	2×10^4	10^5	34.75
	19	4×10^4	10^5	52.02
	20	8×10^4	10^5	57.83
Set C	21	2×10^4	2×10^5	42.88
	22	4×10^4	2×10^5	52.02
	23	8×10^4	2×10^5	78.33
24		4×10^5	10^5	\
25		4×10^6	5×10^4	\

Note. The effusion rate is defined as the overall discharge rate supplied to each single rille (four volcanic vents in total). Both the effusion rate and eruptive duration refer to the constant-effusion-rate episode. Simulations are grouped into three parts: Groups 1–14 (different effusion rates with a consistent eruptive duration), Groups 15–23 (three sets of eruptive durations under specific effusion rates), and Groups 24–25 (extremely high effusion rates).

3.3. Sensitivity Analyses of Input Parameters

Sensitivity analyses were conducted to evaluate how two input parameters—cell width and plane slope—influence the model outcomes (See Text S4, Table S2 and Figure S3–S5 in Supporting Information S1). The tests show that variations in cell width have only a minor effect on the infilled SR length. Although finer grids (cell width of 250 m) better capture channel curvature, they substantially increase computation time by nearly a factor of 10. In contrast, changes in plane slope have a more noticeable impact: gentler slopes favor channel-confined flow, whereas steeper slopes promote longer runout or enhanced overflow depending on the effusion rate. These results indicate that the model behavior is stable across reasonable choices of input parameters.

4. Discussion

4.1. Preservation Potential of Sinuous Rilles

Effusion rate governs how lava flows extend and spread, thereby controlling their geometries and shaping associated landforms (Calvari et al., 2003; Harris et al., 2007; Wadge, 1978; Walker, 1973). In our simulations, the effusion rate of the constant-effusion-rate episode controls the preservation potential of pre-existing sinuous rilles, defining three distinct regimes (Figure 7e). Results indicate that sinuous rilles are most likely to be

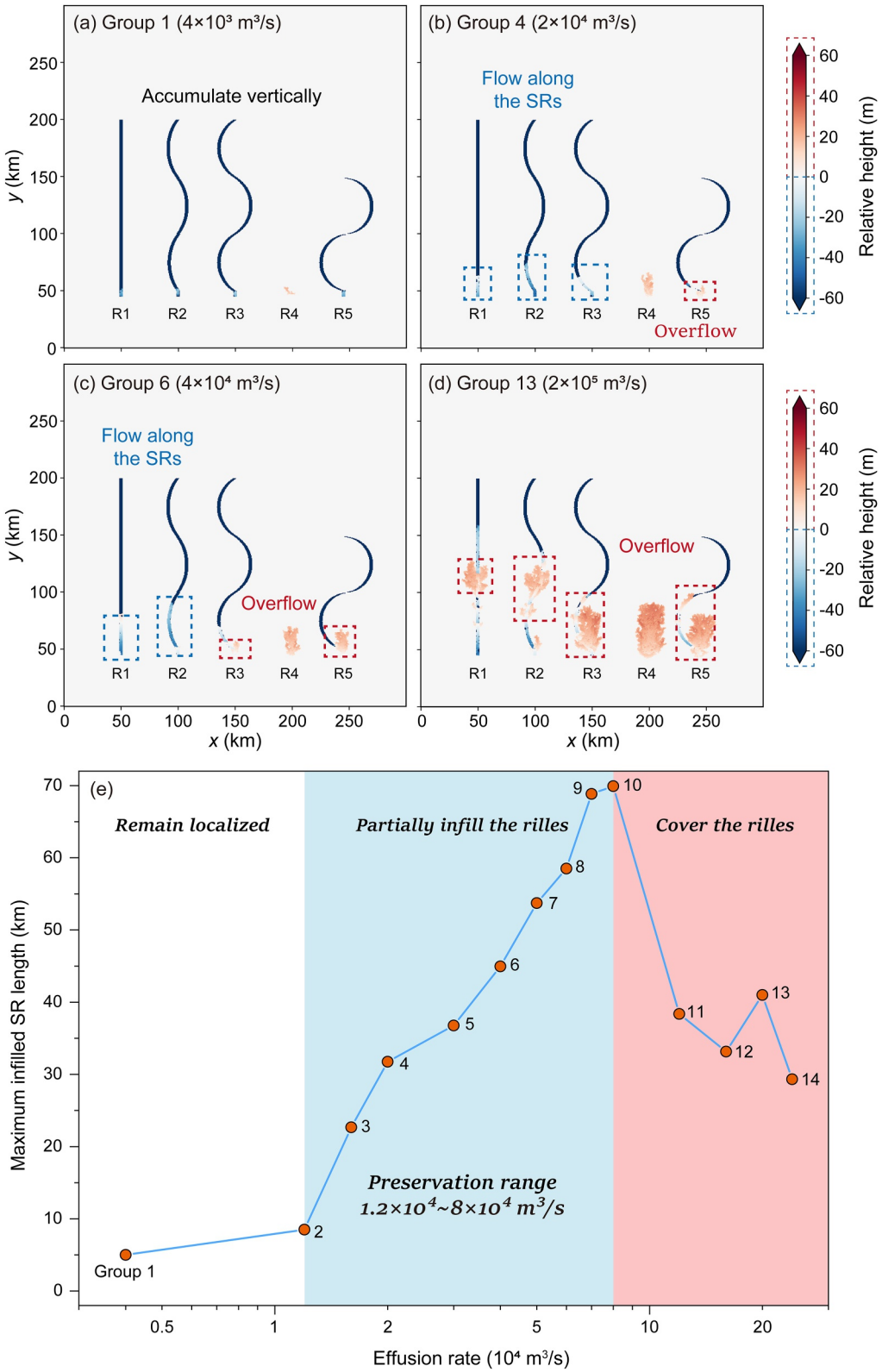

Figure 7.

preserved for effusion rates between 1.2×10^4 and 8×10^4 m^3/s; in these conditions, lava tends to flow within and along the rilles, but does not cover them (Figures 7b and 7c). If the effusion rate exceeds 8×10^4 m^3/s, lava flows tend to bury the rilles, overflowing onto the surrounding surface (Figure 7d). Particularly, the proximal regions of R3 and R5 have been completely buried—a phenomenon consistent with the absence of observable source vents in many rilles (Hurwitz et al., 2013). Conversely, if the effusion rate falls below 1.2×10^4 m^3/s, lava accumulates near the vent and does not laterally advance along the rilles (Figure 7a). These results provide quantitative bounds on the effusion rates that favor rille preservation and thus offer new constraints on the eruptive conditions associated with lunar mare volcanism.

The overflow stage, during which lava overtops a rille after initially infilling it, has been recognized as a key process in modifying volcanic channels (Favalli et al., 2010; Kilburn, 2015; Wadge et al., 2012). In our model, overflow occurs when lava partly fills a rille but its front stalls, and the continued input of lava causes the flow to inflate and overtop the rille. This overflow marks when sinuous rilles become buried rather than preserved, which is reflected by a decrease in the infilled SR length (Figure 8). Two factors hinder lava propagation and could thus promote overflow: *high cooling rate* and *topographical obstruction*. Regarding a high cooling rate, due to the low temperature of the Moon's surface (Williams et al., 2017), lunar lava rapidly cools when it erupts (Griffiths & Fink, 1992). Our simulation results show that the temperature at the flow front rapidly drops below 1240 K (see temperature distribution maps in the Data Set S2 in Supporting Information S3), corresponding to a significant rise in lava yield strength (σ_y) to $\sim 10^4$ Pa (Figure 5). Given that the basal elevation difference (Δz) at the flow front is negligible compared to the thickness variation (Δh), Equation 2 yields a critical thickness (H_c) required for continued motion of ~70 m. This critical thickness of 70 m exceeds the original rille depth (60 m), and indicates that once the forward motion of cooling lava at the flow front is inhibited, newly supplied lava cannot advance further and instead will accumulate at the stalled front, progressively increasing the flow thickness until overtopping the rilles. Therefore, prolonged eruptive durations do not enhance the downstream propagation of lava within the rille but increase the likelihood of overflow due to front stagnation. We find that the upper limit of eruptive duration for the preservation of rilles is about 10^5 s (nearly one day on Earth) (Figure 8b). Beyond this threshold, overflow becomes dominant, leading to a decrease in the infilled SR length (Figure 8c). Topographical obstruction could occur when the local orientation of a rille segment differs significantly from the downslope direction of the plane. We examined the effect of topographical obstruction by testing four different sinuosities (Figure 2). A larger sinuosity (1.6) corresponds to stronger curvature and thus a greater mismatch between the rille direction and downslope direction. In such cases, our models show that a significant portion of lava does not flow along the pre-existing rilles but spills onto the surrounding surface (e.g., R5 in Figures 7c and 7d). Conversely, when the sinuosity is 1.1 and 1.3, the rille direction remains more closely aligned with the downslope direction of the plane, allowing lava flows to stay within the rilles without overflowing. This behavior is attributed to the Bingham fluid nature of lava, making it difficult to flow freely in any direction (Griffiths, 2000). As a result, lava preferentially follows the downslope gravitational gradient rather than adjusting its trajectory to accommodate strong channel curvature. This mechanism explains how variations in rille sinuosities modulate lava flow propagation and consequently influence the preservation potential of sinuous rilles.

4.2. Pulsing Overflow and Sheet Flow

At higher effusion rates, the behavior of lava transitions from single-stage overflow (R1 and R2 in Figure 7d) to pulsing overflow, where repeated surges of lava periodically exceed the rilles and form lateral lobes (R1 and R2 in Figure 9a). While previous studies have attributed this behavior to temporal variations in magma supply (e.g., Bailey et al., 2006; James et al., 2007, 2010), our model maintains a constant effusion rate over time. Therefore, the emergence of pulsing overflow in this context cannot be explained by supply-driven forcing. Instead, we infer that pulsing overflow results from cooling-induced rheological changes during lava

Figure 7. (a–d) Four representative snapshots of Groups 1, 4, 6, and 13 at 2×10^5 s, with effusion rates of 4×10^3, 2×10^4, 4×10^4, and 2×10^5 m^3/s, respectively. The color bar, representing the height relative to the plane, is divided into two parts: the red part with a positive height value indicates that sinuous rilles have been covered by lava, while the blue part with a negative height value represents well-preserved sinuous rilles; (e) Maximum infilled SR lengths change with effusion rates of 14 simulation groups. Numbers shown next to data points indicate the corresponding simulation groups listed in Table 3. The plot reveals three distinct regimes of lava flows: (1) remain localized near vents at low effusion rates ($<1.2 \times 10^4$ m^3/s), (2) flow along and partially infill the rilles at intermediate effusion rates (1.2×10^4–8×10^4 m^3/s), and (3) spill out and cover the rilles at high effusion rates ($>8 \times 10^4$ m^3/s).

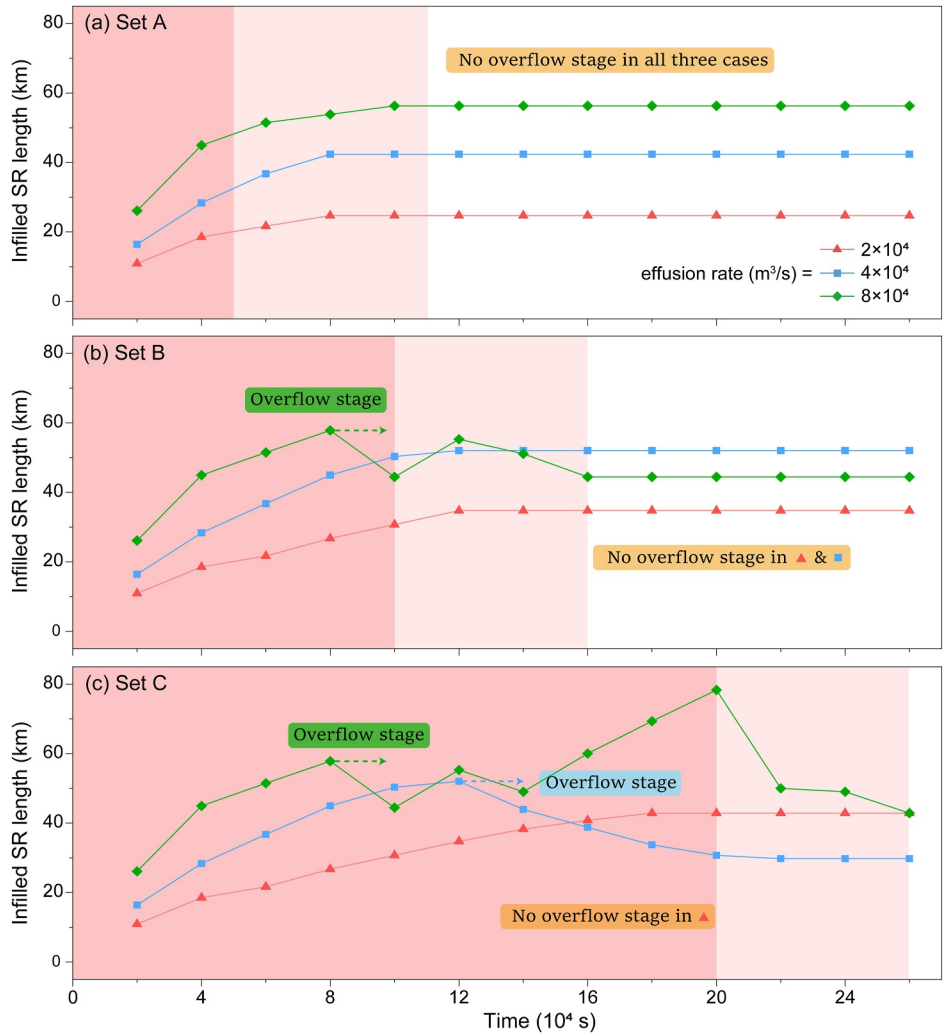

Figure 8. The variation of infilled SR length of rille R2 with time under the eruptive duration of (a) Set A: 5×10^4 s, (b) Set B: 10^5 s and (c) Set C: 2×10^5 s (pink regions), each followed by a decreasing-effusion-rate episode (light-pink regions) lasting 6×10^4 s. Each set contains three runs with different effusion rates: 2×10^4 (red triangle), 4×10^4 (blue square), and 8×10^4 m^3/s (green diamond). Dashed arrows represent the onset of overflow stages.

emplacement, consistent with the overflow mechanism discussed in Section 4.1 and with interpretations proposed by Wadge et al. (2012).

In addition to a pulsing behavior, our simulations reveal a transition to sheet-like flow under conditions of higher effusion rates and increased rille sinuosity (R3 and R5 in Figures 9a and 9b). In these cases, lava no longer remains within the rille but instead totally covers the topography, spreading laterally over the rille. This sheet flow behavior leads to a substantial decrease in both the depth and length of pre-existing sinuous rilles. Notably, the depth of the preserved rille decreased progressively from the proximal to distal regions until it eventually vanished.

4.3. Implications for Lunar Mare Volcanism Change and Thermal Evolution History

Mare volcanism since the Imbrian occurred mainly in two stages (Stage I and IV) (Du et al., 2022; Head et al., 2023; Hiesinger et al., 2011; Tian et al., 2023). We found that the total length of sinuous rilles (~2,100 km) and mare basalt area (~1.6×10^6 km^2) were substantial during the early peak (Stage I, 3.8–3.4 Ga). In the late surge (Stage IV, 2.0–1.2 Ga), the total rille length remained of similar magnitude (~2,500 km), but the corresponding mare area decreased by approximately a factor of three (~5.6×10^5 km^2), resulting in a higher area

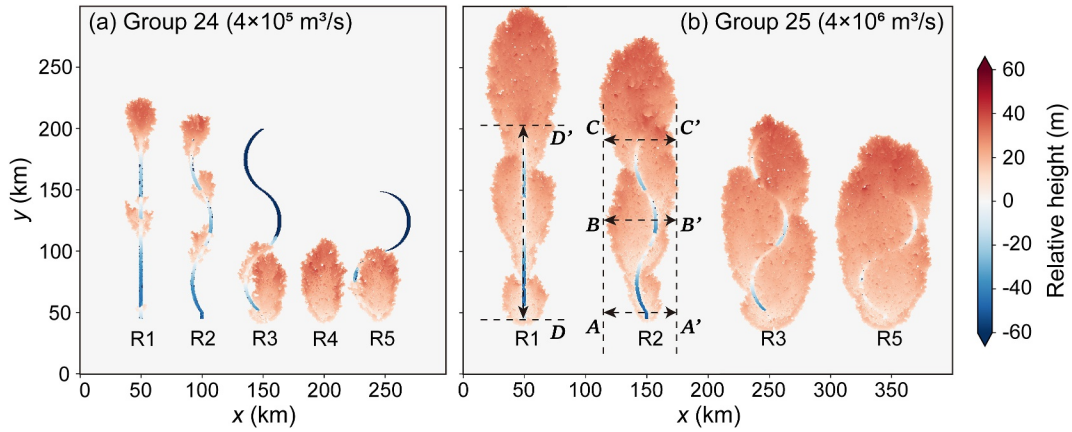

Figure 9. (a) Snapshot of Group 24 at 2×10^5 s, under the effusion rate of 4×10^5 m^3/s with the eruptive duration of 10^5 s. (b) Snapshot of Group 25 at 1.5×10^5 s, under the effusion rate of 4×10^6 m^3/s with the eruptive duration of 5×10^4 s. The dashed lines *AA'*, *BB'* and *CC'* represent cross sections of R2 at distances of 2.5 km, 77.5 km, and 150 km from the vents, while *DD'* represents the longitude section of R1. To improve visual clarity and avoid overlapping among the four lava flows in the output plots, we extended the display canvas to 700 × 600 cells, although all simulations were still performed on a 600 × 600 grid, same as Figure 2.

density—rille length per unit mare basalt area—compared to Stage I (44.9 vs. 13.5 km^{-4} in Figure 1b). This increase in area density suggests that sinuous rilles were better preserved in Stage IV than Stage I, perhaps because there were fewer subsequent vigorous lava flows that could cover the rilles. Specifically, our results suggest that during the late surge of mare volcanism (Stage IV), few rilles formed in the earlier Phase 2 were likely to be covered by subsequent Phase 3 lava flows, particularly if the effusion rate was $<8 \times 10^4$ m^3/s from our modeling results, that is, more rilles were preserved. In contrast, Phase 2 eruptions of Stage I might have led to the formation of numerous rilles, but subsequent Phase 3 intense volcanic activity (with an effusion rate $>10^5$ m^3/s) would fill and cover most rilles. We consider it plausible that the change in the preservation potential of sinuous rilles we show relates to a change in lunar mare volcanism, from an early intense mode to a late mild mode. This change in mare volcanism could indicate gradual cooling of the Moon's interior and reduction in mare magma supply.

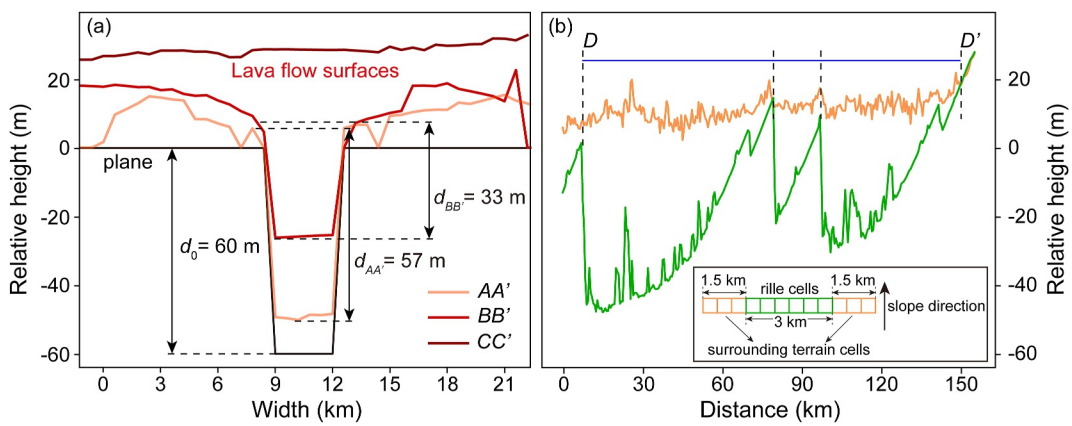

Figure 10. (a) The cross sections of the proximal (*AA'*, light red line), medial (*BB'*, red line), and distal (*CC'*, dark red line) part of lava flows in Figure 9. d_0 represents the initial rille depth, whereas $d_{AA'}$ and $d_{BB'}$ correspond to the rille depths measured at *AA'* and *BB'* cross sections. (b) The longitude section *DD'* in Figure 9. The green line represents the relative height of lava within the sinuous rille, calculated as the average lava thickness across the cells comprising the sinuous rille (green cells in inset). The orange line represents the relative average height of lava spilled over the surrounding terrain on either side (orange cells in inset) of the rille up to 1.5 km away.

5. Conclusion

Sinuous rilles are meandering channel-like depressions formed by highly effusive basaltic lava flows in the lunar maria regions. Assessing their preservation potential can provide insight into the eruptive behaviors of mare volcanism through lunar history. By comparing their distribution with the areal extent of mare basalts, we find that the area density of sinuous rilles—defined as total rille length per unit mare basalt area—is markedly higher in the late surge stage of mare volcanism (2.0–1.2 Ga) than in the early peak stage (3.8–3.4 Ga). This contrast implies that rilles were more effectively preserved in the later stage, even though most rilles and mare basalts were emplaced earlier. Our Cellular Automata model, parameterized using physical properties measured from the Chang'e-5 basalt sample, simulates the flow of lunar basalts and provides a physical explanation for this pattern. Results show that preservation is likely possible only within a specific range of effusion rates (1.2×10^4–8×10^4 m^3/s) and eruptive durations ($<10^5$ s), where lava could flow within rilles instead of overflowing or covering them. Together, the area density analysis and simulation results suggest that the late surge of mare volcanism was characterized by milder eruptions that were less capable of covering earlier-formed rilles, whereas the early stage involved more intense activity that promoted rille burial. This shift from an early intense mode to a later mild one is consistent with progressive cooling of the Moon's interior and declining magma supply. Our conclusions are limited by the two-dimensional nature of the model, the assumption of a single lava composition, and idealized rille geometry; future work incorporating three-dimensional modeling and real-world topography will help refine constraints on rille formation and preservation.

Conflict of Interest

The authors declare no conflicts of interest relevant to this study.

Availability Statement

The codes for the simulation of lava are available for download in the Zenodo repository located at Deng et al. (2024). All the simulation data and results are available for download in the Zenodo repository located at Deng et al. (2025).

Acknowledgments
The authors wish to thank Dr. Meng Tian for his essential suggestions for our manuscripts. This work is supported by the National Key R&D Program of China (Grant 2024YFF0809900), and the National Natural Science Foundation of China (42272348 and 424B2020).

References

Bailey, J. E., Harris, A. J. L., Dehn, J., Calvari, S., & Rowland, S. (2006). The changing morphology of an open lava channel on Mt. Etna. *Bulletin of Volcanology*, *68*(6), 497–515. https://doi.org/10.1007/s00445-005-0025-6

Barca, D., Crisci, G. M., Di Gregorio, S., & Nicoletta, F. (1993). Cellular automata methods for modelling lava flows; simulation of the 1986-1987 eruption, Mount Etna, Sicily. In *Active lavas; monitoring and modelling* (pp. 291–336). UCL Press.

Bilotta, G., Cappello, A., Herault, A., Vicari, A., Russo, G., & Del Negro, C. (2012). Sensitivity analysis of the MAGFLOW Cellular Automaton model for lava flow simulation. *Environmental Modelling and Software*, *35*, 122–131. https://doi.org/10.1016/j.envsoft.2012.02.015

Bottinga, Y., & Weill, D. F. (1970). Densities of liquid silicate systems calculated from partial molar volumes of oxide components. *American Journal of Science*, *269*(2), 169–182. https://doi.org/10.2475/ajs.269.2.169

Calvari, S., Neri, M., & Pinkerton, H. (2003). Effusion rate estimations during the 1999 summit eruption on Mount Etna, and growth of two distinct lava flow fields. *Journal of Volcanology and Geothermal Research*, *119*(1–4), 107–123. https://doi.org/10.1016/S0377-0273(02)00308-6

Cappello, A., Bilotta, G., & Ganci, G. (2022). Modeling of geophysical flows through GPUFLOW. *Applied Sciences*, *12*(9), 4395. https://doi.org/10.3390/app12094395

Carrier, W. D., III, Olhoeft, G. R., & Mendell, W. (1991). Physical properties of the lunar surface. In *Lunar sourcebook, a user's guide to the moon* (pp. 475–594).

Courant, R., Friedrichs, K., & Lewy, H. (1928). Über die partiellen Differenzengleichungen der mathematischen Physik. *Mathematische Annalen*, *100*(1), 32–74. https://doi.org/10.1007/bf01448839

Crisci, G. M., Gregorio, D., Pindaro, O., & Ranieri, G. A. (1986). Lava flow simulation Bv A discrete cellular model: First implementation. *International Journal of Modelling and Simulation*, *6*(4), 137–140. https://doi.org/10.1080/02286203.1986.11759975

Deng, X., Tian, W., Qian, Y., Magee, C., Gao, Z., Wei, Z., et al. (2024). "LavaSim" codes from Deng et al. (2025) "Secular Change of Preservation of Lunar Sinuous Rilles: Constraints from Lava Flow Numerical Modeling" (v1.0.1) [Software]. *Zenodo*. https://doi.org/10.5281/zenodo.14381640

Deng, X., Tian, W., Qian, Y., Magee, C., Gao, Z., Wei, Z., et al. (2025). Data from Deng et al. (2025) "Secular Change of Preservation of Lunar Sinuous Rilles: Constraints from Lava Flow Numerical Modeling" (v3) [Dataset]. *Zenodo*. https://doi.org/10.5281/zenodo.17989122

Dragoni, M. (1989). A dynamical model of lava flows cooling by radiation. *Bulletin of Volcanology*, *51*(2), 88–95. https://doi.org/10.1007/Bf01081978

Dragoni, M., Bonafede, M., & Boschi, E. (1986). Downslope flow models of a Bingham liquid: Implications for lava flows. *Journal of Volcanology and Geothermal Research*, *30*(3), 305–325. https://doi.org/10.1016/0377-0273(86)90059-4

Du, J., Fa, W., Gong, S., Liu, Y., Qiao, L., Tai, Y., et al. (2022). Thicknesses of mare basalts in the Chang'E-5 landing Region: Implications for the late-stage volcanism on the Moon. *Journal of Geophysical Research: Planets*, *127*(8), e2022JE007314. https://doi.org/10.1029/2022je007314

Favalli, M., Fornaciai, A., Mazzarini, F., Harris, A., Neri, M., Behncke, B., et al. (2010). Evolution of an active lava flow field using a multitemporal LiDAR acquisition. *Journal of Geophysical Research*, *115*(B11), B11203. https://doi.org/10.1029/2010jb007463

Ghiorso, M. S., Hirschmann, M. M., Reiners, P. W., & Kress, V. C. (2002). The pMELTS: A revision of MELTS for improved calculation of phase relations and major element partitioning related to partial melting of the mantle to 3 GPa. *Geochemistry, Geophysics, Geosystems*, *3*(5), 1–35. https://doi.org/10.1029/2001gc000217

Giordano, D., Russell, J. K., & Dingwell, D. B. (2008). Viscosity of magmatic liquids: A model. *Earth and Planetary Science Letters*, *271*(1–4), 123–134. https://doi.org/10.1016/j.epsl.2008.03.038

Greeley, R. (1971). Lava tubes and channels in the lunar Marius Hills. *The Moon*, *3*(3), 289–314. https://doi.org/10.1007/bf00561842

Griffiths, R. W. (2000). The dynamics of lava flows. *Annual Review of Fluid Mechanics*, *32*(1), 477–518. https://doi.org/10.1146/annurev.fluid.32.1.477

Griffiths, R. W., & Fink, J. H. (1992). The morphology of lava flows in planetary environments: Predictions from analog experiments. *Journal of Geophysical Research*, *97*(B13), 19739–19748. https://doi.org/10.1029/92jb01953

Gudmundsson, A. (2020). *Volcanotectonics: Understanding the structure, deformation, and dynamics of volcanoes*. Cambridge University Press. https://doi.org/10.1017/9781139176217

Harris, A. J., & Rowland, S. K. (2015). Lava flows and rheology. In *The encyclopedia of volcanoes* (2 ed., pp. 321–342). Elsevier. https://doi.org/10.1016/B978-0-12-385938-9.00017-1

Harris, A. J. L., Dehn, J., & Calvari, S. (2007). Lava effusion rate definition and measurement: A review. *Bulletin of Volcanology*, *70*, 1–22. https://doi.org/10.1007/s00445-007-0120-y

Harris, A. J. L., Murray, J. B., Aries, S. E., Davies, M. A., Flynn, L. P., Wooster, M. J., et al. (2000). Effusion rate trends at Etna and Krafla and their implications for eruptive mechanisms. *Journal of Volcanology and Geothermal Research*, *102*(3–4), 237–269. https://doi.org/10.1016/S0377-0273(00)00190-6

Head, J. W., & Wilson, L. (1992). Lunar Mare volcanism: Stratigraphy, eruption conditions, and the evolution of secondary crusts. *Geochimica et Cosmochimica Acta*, *56*(6), 2155–2175. https://doi.org/10.1016/0016-7037(92)90183-J

Head, J. W., Wilson, L., Hiesinger, H., van der Bogert, C., Chen, Y., Dickson, J. L., et al. (2023). Lunar mare basaltic volcanism: Volcanic features and emplacement processes. *Reviews in Mineralogy and Geochemistry*, *89*(1), 453–507. https://doi.org/10.2138/rmg.2023.89.11

Hiesinger, H., Head, J. W., Wolf, U., Jaumann, R., & Neukum, G. (2011). Ages and stratigraphy of lunar mare basalts: A synthesis. In *Recent advances and Current research issues in lunar stratigraphy* (Vol. 477, pp. 1–51). Geological Society of America Special Paper. https://doi.org/10.1130/2011.2477(01

Hurwitz, D. M., Head, J. W., & Hiesinger, H. (2013). Lunar sinuous rilles: Distribution, characteristics, and implications for their origin. *Planetary and Space Science*, *79–80*, 1–38. https://doi.org/10.1016/j.pss.2012.10.019

Hurwitz, D. M., Head, J. W., Wilson, L., & Hiesinger, H. (2012). Origin of lunar sinuous rilles: Modeling effects of gravity, surface slope, and lava composition on erosion rates during the formation of Rima Prinz. *Journal of Geophysical Research*, *117*(E12), E00H14. https://doi.org/10.1029/2011je004000

James, M. R., Pinkerton, H., & Ripepe, M. (2010). Imaging short period variations in lava flux. *Bulletin of Volcanology*, *72*(6), 671–676. https://doi.org/10.1007/s00445-010-0354-y

James, M. R., Pinkerton, H., & Robson, S. (2007). Image-based measurement of flux variation in distal regions of active lava flows. *Geochemistry, Geophysics, Geosystems*, *8*(3). https://doi.org/10.1029/2006gc001448

Keihm, S. J. (1984). Interpretation of the lunar microwave brightness temperature spectrum: Feasibility of orbital heat flow mapping. *Icarus*, *60*(3), 568–589. https://doi.org/10.1016/0019-1035(84)90165-9

Kilburn, C. R. (2015). Lava flow hazards and modeling. In *The encyclopedia of volcanoes* (2 ed., pp. 957–969). Elsevier. https://doi.org/10.1016/B978-0-12-385938-9.00055-9

Leroux, J. P. (1992). Determining the channel sinuosity of Ancient fluvial systems from paleocurrent Data. *Journal of Sedimentary Petrology*, *62*(2), 283–291. https://doi.org/10.1306/D42678E3-2B26-11D7-8648000102C1865D

Lin, H. L., Xu, R., Li, S., Chang, R., Hui, H. J., Liu, Y., et al. (2024). Higher water content observed in smaller size fraction of Chang'e-5 lunar regolith samples. *Science Bulletin*, *69*(23), 3723–3729. https://doi.org/10.1016/j.scib.2024.05.031

Liu, J. J., Liu, B., Ren, X., Li, C. L., Shu, R., Guo, L., et al. (2022). Evidence of water on the lunar surface from Chang'E-5 in-situ spectra and returned samples. *Nature Communications*, *13*(1), 3119. https://doi.org/10.1038/s41467-022-30807-5

Liu, Y. (2020). Maximizing the CFL number of stable time-space domain explicit finite-difference modeling. *Journal of Computational Physics*, *416*, 109501. https://doi.org/10.1016/j.jcp.2020.109501

Luo, B. J., Wang, Z. C., Song, J. L., Qian, Y. Q., He, Q., Li, Y. H., et al. (2023). The magmatic architecture and evolution of the Chang'e-5 lunar basalts. *Nature Geoscience*, *16*(4), 301–308. https://doi.org/10.1038/s41561-023-01146-x

Machado, F. (1974). The search for magmatic reservoirs. In *Developments in solid Earth geophysics* (Vol. 6, pp. 255–273). Elsevier. https://doi.org/10.1016/B978-0-444-41141-9.50017-6

Miyamoto, H., & Sasaki, S. (1997). Simulating lava flows by an improved cellular automata method. *Computers and Geosciences*, *23*(3), 283–292. https://doi.org/10.1016/S0098-3004(96)00089-1

Neri, A. (1998). A local heat transfer analysis of lava cooling in the atmosphere: Application to thermal diffusion-dominated lava flows. *Journal of Volcanology and Geothermal Research*, *81*(3–4), 215–243. https://doi.org/10.1016/S0377-0273(98)00010-9

Ortega-Moya, J., Martínez-Aranda, S., Fernández-Pato, J., & García-Navarro, P. (2024). A vertically non-uniform temperature approach for the friction term computation in depth-averaged viscoplastic lava flows. *Journal of Computational Physics*, *519*, 113378. https://doi.org/10.1016/j.jcp.2024.113378

Qian, Y. Q., She, Z. B., He, Q., Xiao, L., Wang, Z. C., Head, J. W., et al. (2023). Mineralogy and chronology of the young mare volcanism in the Procellarum-KREEP-Terrane. *Nature Astronomy*, *7*(3), 287–297. https://doi.org/10.1038/s41550-022-01862-1

Qian, Y. Q., Xiao, L., Head, J. W., van der Bogert, C. H., Hiesinger, H., & Wilson, L. (2021). Young lunar mare basalts in the Chang'e-5 sample return region, northern Oceanus Procellarum. *Earth and Planetary Science Letters*, *555*, 116702. https://doi.org/10.1016/j.epsl.2020.116702

Qian, Y. Q., Xiao, L., Head, J. W., & Wilson, L. (2021). The long sinuous rille System in Northern oceanus procellarum and its relation to the Chang'e-5 returned samples. *Geophysical Research Letters*, *48*(11), e2021GL092663. https://doi.org/10.1029/2021GL092663

Roberts, C. E., & Gregg, T. K. P. (2019). Rima Marius, the Moon: Formation of lunar sinuous rilles by constructional and erosional processes. *Icarus*, *317*, 682–688. https://doi.org/10.1016/j.icarus.2018.02.033

Robson, G. R. (1967). Thickness of etnean Lavas. *Nature*, *216*(5112), 251–252. https://doi.org/10.1038/216251a0

Shearer, C. K., Hess, P. C., Wieczorek, M. A., Pritchard, M. E., Parmentier, E. M., Borg, L. E., et al. (2006). Thermal and magmatic evolution of the moon. *New Views of the Moon*, *60*, 365–518. https://doi.org/10.2138/rmg.2006.60.4

Spohn, T., Konrad, W., Breuer, D., & Ziethe, R. (2001). The longevity of lunar volcanism: Implications of thermal evolution calculations with 2D and 3D mantle convection models. *Icarus*, *149*(1), 54–65. https://doi.org/10.1006/icar.2000.6514

Thordarson, T., & Larsen, G. (2007). Volcanism in Iceland in historical time: Volcano types, eruption styles and eruptive history. *Journal of Geodynamics*, *43*(1), 118–152. https://doi.org/10.1016/j.jog.2006.09.005

Tian, H. C., Zhang, C., Yang, W., Du, J., Chen, Y., Xiao, Z., et al. (2023). Surges in volcanic activity on the Moon about two billion years ago. *Nature Communications*, *14*(1), 3734. https://doi.org/10.1038/s41467-023-39418-0

Turcotte, D., & Schubert, G. (2014). *Geodynamics* (3 ed.). Cambridge University Press. https://doi.org/10.1017/CBO9780511843877

Vicari, A., Alexis, H., Del Negro, C., Coltelli, M., Marsella, M., & Proietti, C. (2007). Modeling of the 2001 lava flow at Etna volcano by a Cellular Automata approach. *Environmental Modelling and Software*, *22*(10), 1465–1471. https://doi.org/10.1016/j.envsoft.2006.10.005

Wadge, G. (1978). Effusion rate and the shape of aa lava flow-fields on Mount Etna. *Geology*, *6*(8), 503–506. https://doi.org/10.1130/0091-7613(1978)6<503:ERATSO>2.0.CO;2

Wadge, G., Saunders, S., & Itikarai, I. (2012). Pulsatory andesite lava flow at Bagana Volcano. *Geochemistry, Geophysics, Geosystems*, *13*(11), Q11011. https://doi.org/10.1029/2012gc004336

Walker, G. P. L. (1973). Lengths of lava flows. *Philosophical Transactions of the Royal Society A: Mathematical, Physical & Engineering Sciences*, *274*(1238), 107–118. https://doi.org/10.1098/rsta.1973.0030

Wang, Z. L., Wang, W., Tian, W., Li, H. J., Qian, Y. Q., Pei, J. L., et al. (2023). Cooling rate of clinopyroxene reveals the thickness and effusion volume of Chang'E-5 basaltic flow units. *Icarus*, *394*, 115406. https://doi.org/10.1016/j.icarus.2022.115406

Williams, D. A., Fagents, S. A., & Greeley, R. (2000). A reassessment of the emplacement and erosional potential of turbulent, low-viscosity lavas on the Moon. *Journal of Geophysical Research*, *105*(E8), 20189–20205. https://doi.org/10.1029/1999je001220

Williams, J. P., Paige, D. A., Greenhagen, B. T., & Sefton-Nash, E. (2017). The global surface temperatures of the moon as measured by the diviner lunar radiometer experiment. *Icarus*, *283*, 300–325. https://doi.org/10.1016/j.icarus.2016.08.012

Wilson, L., & Head, J. W. (2017). Generation, ascent and eruption of magma on the Moon: New insights into source depths, magma supply, intrusions and effusive/explosive eruptions (part 1: Theory). *Icarus*, *283*, 146–175. https://doi.org/10.1016/j.icarus.2015.12.039

Wilson, L., & Head, J. W. (2018). Controls on lunar basaltic volcanic eruption structure and morphology: Gas release patterns in sequential eruption phases. *Geophysical Research Letters*, *45*(12), 5852–5859. https://doi.org/10.1029/2018gl078327

Xiao, X., Yu, S. R., Huang, J., Zhang, H., Zhang, Y. W., & Xiao, L. (2022). Thermophysical properties of the regolith on the lunar far side revealed by the temperature probing of the Chang'E-4 mission. *National Science Review*, *9*(11), nwac175. https://doi.org/10.1093/nsr/nwac175

Yu, S. R., & Fa, W. Z. (2016). Thermal conductivity of surficial lunar regolith estimated from Lunar Reconnaissance Orbiter Diviner Radiometer data. *Planetary and Space Science*, *124*, 48–61. https://doi.org/10.1016/j.pss.2016.02.001